ACADEMIC PRESS

Available online at www.sciencedirect.com

SCIENCE DIRECT®

Analytical Biochemistry 317 (2003) 186–200

ANALYTICAL BIOCHEMISTRY

www.elsevier.com/locate/yabio

Modeling of DNA hybridization kinetics for spatially resolved biochips

David Erickson,[a] Dongqing Li,[a,*] and Ulrich J. Krull[b]

[a] *Department of Mechanical and Industrial Engineering, University of Toronto, 5 King's College Road, Toronto, Ont. M5S 3G8, Canada*
[b] *Chemical Sensors Group, Department of Chemistry, University of Toronto at Mississauga, 3359 Mississauga Road North, Mississauga, Ont. L5L 1C6, Canada*

Received 27 November 2002

Abstract

The marriage of microfluidics with detection technologies that rely on highly selective nucleic acid hybridization will provide improvements in bioanalytical methods for purposes such as detection of pathogens or mutations and drug screening. The capability to deliver samples in a controlled manner across a two-dimensional hybridization detection platform represents a substantial technical challenge in the development of quantitative and reusable biochips. General theoretical and numerical models of heterogeneous hybridization kinetics are required in order to design and optimize such biochips and to develop a quantitative method for online interpretation of experimental results. In this work we propose a general kinetic model of heterogeneous hybridization and develop a technique for estimating the kinetic coefficients for the case of well-spaced, noninteracting surface-bound probes. The experimentally verified model is then incorporated into the BLOCS (biolab-on-a-chip simulation) 3D microfluidics finite element code and used to model the dynamic hybridization on a biochip surface in the presence of a temperature gradient. These simulations demonstrate how such a device can be used to discriminate between fully complementary and single-base-pair mismatched hybridization using fluorescence detection by interpretation of the unique spatially resolved intensity pattern. It is also shown how the dynamic transport of the targets is likely to affect the rate and location of hybridization as well as that, although nonspecific hybridization is present, the change in the concentration of hybridized targets over the sensor platform is sufficiently high to determine if a fully complementary match is present. Practical design information such as the optimum transport speed, target concentration, and channel height is presented. The results presented here will aid in the interpretation of results obtained with such a temperature-gradient biochip.

Keywords: Biochips; Biosensors; DNA; Hybridization; Finite element method; Fluorescence

Biosensors and, more specifically, biochips exploit the interactions between a target analyte and an immobilized biological recognition element to produce a measurable signal (visual, fluorescent, or electrical), which can be interpreted to gain valuable information regarding the presence and concentration of the target. Fundamentally the sensitivity and detection limits of such devices are limited by the degree to which they can discriminate between selective binding of the target analyte and nonselective binding by chemical interferents. Systems based on solid-phase nucleic acid hybridization such as those encountered in the area of DNA biosensors [1–5] are particularly attractive due to the high degree of selectivity in the binding interactions and the relatively facile integration of the sensing chemistry with the transduction element [6,7]. It is well known that when using these devices, interference due to nonselective binding can be controlled through manipulation of the stringency conditions. It is possible to achieve excellent selectivity control in some cases by exploiting the differences in the thermodynamic stability of a fully complementary duplex and one containing a single or multiple base-pair mismatch [8]. A fundamental understanding of the kinetics and thermodynamics of solid-phase DNA hybridization and the

* Corresponding author. Fax: 416-978-7753.
E-mail address: dli@mie.utoronto.ca (D. Li).

0003-2697/03/$ - see front matter © 2003 Elsevier Science (USA). All rights reserved.
doi:10.1016/S0003-2697(03)00090-3

development of advanced mathematical and numerical models to interpret/predict experimental results is necessary in order to design and optimize spatially resolved detectors in biochips.

A number of reports have appeared regarding the experimental examination of the real-time kinetics and equilibrium thermodynamics of solid-phase oligonucleotide hybridization using a wide variety of techniques and probe–target complexes. Koval et al. [9] used a resonant mirror technique to determine kinetic association and dissociation constants for an 11-mer and 14-mer oligonucleotide set. Okahata et al. [10] used a quartz crystal microbalance to examine the hybridization kinetics of 10-, 20-, and 30-mer oligonucleotides in a variety of salt solutions. Jobs et al. [11] examined the effects of oligonucleotide truncation on base-pair mismatches at various temperatures. Riccelli et al. [12] examined the kinetic and stability benefits of using hairpin probes vs traditional linear probes. Yguerabide and Ceballos [13] studied hybridization kinetics using a fluorescent intercalator. In their studies, Stevens et al. [14] and Henry et al. [15] used a fluorescence energy transfer technique to examine hybridization on microparticles. They observed that the rate of hybridization decreased with increasing surface probe density, a finding that is consistent with the results of Peterson et al. [16]. Krull et al. [6–8,17] have also investigated the influence of surface probe density, temperature, and salt concentration on the selectivity coefficients and melting temperature of fully complementary and single-base-pair mismatched 20-mer oligonucleotide strands revealing, among other things, that higher surface probe density can increase the selectivity of a biosensor. In a recent study [18] this group has also examined hybridization and adsorption kinetics using an optical fiber sensor. Bier et al. [19] examined the stability of single-base-pair mismatches for a series of 13-mer oligonucleotides using an evanescent-wave sensor. While both association and dissociation kinetic constants were affected by the presence of a base-pair mismatch, the change in the dissociation constant was found to vary more significantly. This is consistent with the findings of Forman et al. [20], who observed that the initial rate of hybridization was not largely affected by the presence of a mismatch.

Compared with experimental investigations there have been, to our knowledge, relatively few attempts at developing comprehensive models of hybridization kinetics. Classically, solid-phase hybridization as related to Southern blotting techniques, for example, [see 21–24 for reviews], has been modeled using the Wetmur and Davidson relationship [25] originally intended for bulk-phase hybridization. While useful in predicting how changes in probe–target length and complexity may affect the rate of hybridization, it is in principle not fully applicable to solid-phase hybridization. Likely the most well cited work about modeling solid-phase hybridization kinetics for biochip applications was presented by Chan et al. [26], based on the receptor–ligand model developed by Axlerod and Wang [27]. In these works it is proposed that hybridization could occur by either of two mechanisms: direct hybridization from the bulk phase or hybridization after an initial nonspecific adsorption step followed by subsequent surface diffusion to the probe. Though strictly applicable to only the initial stages of hybridization and static in nature, this model did predict effects such as the aforementioned enhanced reaction rate at lower surface probe spacing. Based on this approach Zeng et al. [18] used a dynamic model combining two mechanisms as a method of analyzing their hybridization data. As an alternative approach, Ramakrishnan has used fractal kinetics [28] as a method of data analysis. Some models which couple transport relations with surface-phase hybridization have been presented [29,30]. However, these have been generally limited to gel-immobilized oligonucleotides and have not considered the two-mechanism reaction that has appeared in more detailed models. To date there lacks a comprehensive model for heterogeneous hybridization kinetics that can be applied to provide quantitative dynamic predictions of heterogeneous hybridization for biochip applications.

In this paper we present a comprehensive model of dynamic solid-phase oligonucleotide hybridization kinetics, based on an approach that accounts for both the direct hybridization from the bulk phase and the hybridization after an initial nonspecific adsorption step, which is then coupled with a convection–diffusion transport formulation. In the next section, the general theory and equations of the proposed kinetic model will be presented. A technique for estimating the kinetic variables for the special case of well-spaced noninteracting surface probes is then developed. In the Experimental validation section, the proposed theory is compared with experimental results for validation. Finally in the Finite element simulations section of hybridization on temperature gradient surfaces, the model is incorporated into the 3D BLOCS[1] (biolab-on-a-chip simulation) finite element microfluidics code [31] and is used to model the dynamic on-chip hybridization kinetics of a biosensor surface with an applied temperature gradient. The results demonstrate the potential of this approach to sensor development for discriminating between complementary and single-base-pair mismatch hybridization and provides practical biochip design information obtained from numerical experimentation. Important variables are explained as they are introduced; however, a summary of the nomenclature used here is also provided in the Appendix A.

[1] *Abbreviation used:* BLOCS, biolab-on-a-chip simulation.

General theory of coupled transport and surface hybridization/adsorption kinetics

The proposed model is based upon hybridization by either of two mechanisms: direct hybridization from the bulk phase to the surface-bound probes or indirect hybridization in which the target is initially nonspecifically adsorbed on the surface and then diffuses along the surface before reaching an available probe molecule. These processes are detailed in Fig. 1a. In this section the classical transport equations are introduced, followed by a more detailed discussion of the surface-phase kinetics.

Bulk-phase transport

Within the bulk phase, transport of the targets is considered using the traditional convection–diffusion equation,

$$\frac{\partial c_3}{\partial t} + v \cdot \nabla c_3 = D_3 \nabla^2 c_3, \tag{1}$$

where c_3, t, D_3, and v are: concentration of solution-phase targets, time, three-dimensional (i.e., liquid phase) diffusion coefficient, and velocity. For the purposes of this study we ignore electrophoritic transport; however, this can easily be incorporated into the above formulation as was done by Erickson and Li [31]. The combination of specific hybridization and nonspecific adsorption is represented mathematically by the boundary condition shown below, applied at all reacting surfaces,

$$D_3 \nabla c_3 \cdot n = \frac{\partial c_{2,\mathrm{s}}}{\partial t} + \frac{\partial c_{2,\mathrm{ns}}}{\partial t}, \tag{2}$$

where $c_{2,\mathrm{s}}$ and $c_{2,\mathrm{ns}}$ are the surface-phase concentrations of specifically (hybridized) and nonspecifically adsorbed target molecules, respectively, and n is the normal to the surface. Along nonreacting surfaces Eq. (2) reduces to a zero-flux boundary condition since both $\partial c_{2,\mathrm{s}}/\partial t$ and $\partial c_{2,\mathrm{ns}}/\partial t$ are zero at all times. Other boundary conditions are geometry and situation specific and thus will be discussed in later sections when applicable.

Surface-phase kinetics

For the surface kinetics, a set of two-dimensional, coupled kinetic equations is proposed. The first, Eq. (3a), describes the change in the surface concentration of hybridized species as being proportional to the rate of targets becoming hybridized directly from the bulk phase and the rate of targets becoming hybridized after an initial nonspecific adsorption step. Eq. (3b) describes the rate of change in the surface concentration of nonspecifically adsorbed species as being proportional to the rate of adsorption from the bulk phase (using a Langmuirian model as will be described later) and decreasing

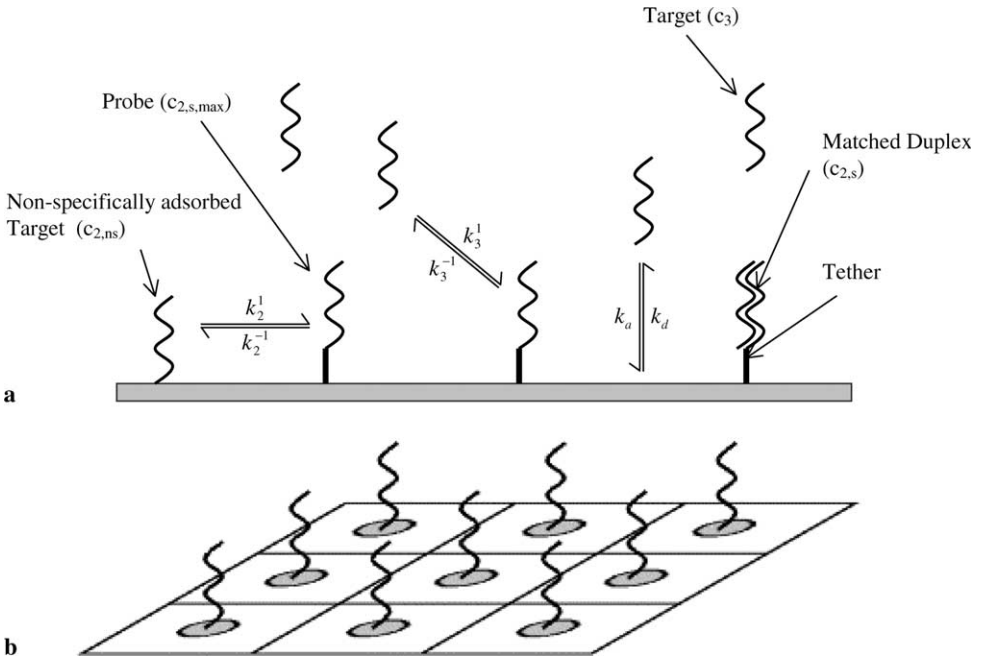

Fig. 1. (a) Schematic representation of proposed solid-phase DNA hybridization model. Kinetic and concentration variables shown are used in Eqs. (3a) and (3b). k_3^1 and k_3^{-1} represent hybridization and denaturation of targets from the bulk phase, k_2^1 and k_2^{-1} represent hybridization and denaturation of the nonspecifically adsorbed targets, and k_a and k_d represent the reversible nonspecific adsorption and desorption of the targets to the surface. $c_{2,\mathrm{s,max}}$ represents the total surface concentration of probes, $c_{2,\mathrm{s}}$ represents the surface concentration of hybridized probes, $c_{2,\mathrm{ns}}$ represents the concentration of nonspecifcally adsorbed targets, and c_3 represents the bulk concentration of targets. (b) Local section of immobilized probe array. Gray circles represent effective probe area and squares represent area per probe.

by a rate at which the nonspecifically adsorbed species become hybridized. Additionally the effects of induced surface mobility due to local concentration variations (due to changes in the probe density or temperature along the sensor surface for example) are accounted for through a surface diffusion term,

$$\frac{\partial c_{2,\mathrm{s}}}{\partial t} = \left[k_3^1 c_{3,\mathrm{m}}(c_{2,\mathrm{s,max}} - c_{2,\mathrm{s}}) - k_3^{-1} c_{2,\mathrm{s}}\right] + \left[k_2^1 c_{2,\mathrm{ns}}(c_{2,\mathrm{s,max}} - c_{2,\mathrm{s}}) - k_2^{-1} c_{2,\mathrm{s}}\right], \tag{3a}$$

$$\frac{\partial c_{2,\mathrm{ns}}}{\partial t} = \left[D_2 \nabla^2 c_{2,\mathrm{ns}}\right] + \left[k_\mathrm{a} c_{3,\mathrm{m}}(c_{2,\mathrm{ns,max}} - c_{2,\mathrm{ns}}) - k_\mathrm{d} c_{2,\mathrm{ns}}\right] - \left[k_2^1 c_{2,\mathrm{ns}}(c_{2,\mathrm{s,max}} - c_{2,\mathrm{s}}) - k_2^{-1} c_{2,\mathrm{s}}\right], \tag{3b}$$

where $c_{2,\mathrm{s,max}}$ is the maximum concentration of hybridized targets, equivalent to the local concentration of surface-bound probes available for hybridization; $c_{2,\mathrm{ns,max}}$ is the maximum concentration of nonspecifically adsorbed molecules, which is calculated based on a theoretical maximum as will be described later; and $c_{3,\mathrm{m}}$ is the bulk-phase concentration of targets in the surface film (i.e., at the mathematical boundary). The first term in square brackets on the right-hand side of Eq. (3a) represents a second order direct hybridization reaction (from the bulk-phase directly to the surface-bound probes). The first order denaturation, which leads to the targets returning to the bulk phase, is governed by the kinetic variables k_3^1 and k_3^{-1}, respectively. The second term accounts for the hybridization and denaturation of the nonspecifically adsorbed targets and is governed by the kinetic variables k_2^1 and k_2^{-1}. The first term in Eq. (3b) accounts for changes in the local surface concentration due to surface diffusion. The second term represents the reversible nonspecific adsorption–desorption of the targets to the surface, governed by the kinetic variables k_a and k_d. The third term in this equation is the term complementary to the second term in Eq. (3a) and accounts for the deficit of the nonspecifically adsorbed targets as they hybridize with surface probes. The reaction orders in the above equations were chosen to represent the simplest possible model consistent with the theory to be developed in subsequent sections. The possibility of using higher order reaction models to yield a better fit with experimental results is explored further in the Hybridization on optical fibers section.

This formulation represents a complete general model applicable to most heterogeneous hybridization situations. It is, however, reliant on the assumption that the six kinetic variables, k_3^1, k_3^{-1}, k_2^1, k_2^{-1}, k_a, and k_d, and their dependence on temperature, salt concentration, and probe density, are known in advance or can be determined experimentally. In the following section we propose a technique based on a combination of collision theory kinetics and previously published experimental data for estimating the value of these constants in the case of well-spaced, noninterfering surface-bound probes.

Theory of hybridization kinetics for well-spaced probes

Collision approach to direct and indirect hybridization kinetics

At a microscopic level the probe molecules can be considered to have a locally uniform pattern (this does not negate the possibility of investigating globally nonuniform probe spacing) similar to that shown in Fig. 1b. The reaction rate for direct hybridization, R_3, as shown in Eq. (4), is given by the flux of bulk-phase target molecules that collide with the surface, F_3, multiplied by the probability that the collision location is a probe site, P_p, the probability that that probe is available for hybridization, P_a, (i.e., it has not yet undergone hybridization with another target), and finally the probability that the collision will result in successful hybridization, P_r,

$$R_3 = F_3 P_\mathrm{p} P_\mathrm{a} P_\mathrm{r}. \tag{4}$$

It can be shown that for a Brownian particle the rate of collisions between a bulk solution of concentration $c_{3,\mathrm{m}}$ and a solid wall of unit surface area is given by Eq. (5) [32],

$$F_3 = \frac{\langle v \rangle_3 c_{3,\mathrm{m}}}{4}, \tag{5}$$

where $\langle v \rangle_3$ is the instantaneous speed of the Brownian target (averaged over the Maxwellian distribution of speeds). For pure diffusion, $\langle v \rangle_3$ is infinite. However, for Brownian motion it is finite and equal to the frequency of collision, σ_n, multiplied by the run between collisions, ζ_n, (or more appropriately for liquids, the Brownian persistence distance, see Axelrod and Wang [27]),

$$\langle v \rangle_n = \zeta_n \sigma_n, \tag{6}$$

where n is the dimensionality. The frequency of collisions can be related to the diffusion coefficient by Eq. (7),

$$D_n = \frac{\zeta_n \sigma_n^2}{2n}. \tag{7}$$

From Eqs. (5)–(7), a new expression for F_3 can be determined as

$$F_3 = \frac{3 D_3 c_{3,\mathrm{m}}}{2\sigma_3} \tag{8}$$

which represents the rate at which molecules collide with a surface of unit area. For hybridization to occur the collision must take place at a probe location, which is a function of the surface probe density (as can be deduced from Fig. 1b),

$$P_p = \frac{A_p}{A_t} = \frac{\pi R_p^2}{1/c_{2,s,max} N_v} = \pi R_p^2 c_{2,s,max} N_v, \quad (9)$$

where R_p is the radius of the probe site, N_v is Avagadro's number, A_p is the area of a probe site, and A_t is the total area per probe (the squares in Fig. 1b). The probability that the probe site is available for hybridization is governed by whether the probe site has already formed a duplex with another target. This probability is given by Eq. (10),

$$P_a = \frac{(c_{2,s,max} - c_{2,s})}{c_{2,s,max}}. \quad (10)$$

Finally, P_r is the probability that a reaction will occur given a collision of a target with an available probe molecule. For now this will be left as an undetermined function represented by χ_3, to be consistent with the terminology of other authors [26,27]. These considerations yield the following equation for the rate of reaction,

$$R_3 = \left[\frac{3D_3 N_v \pi R_p^2 \chi_3}{2\sigma_3}\right] c_{3,m}(c_{2,s,max} - c_{2,s}) = k_3^1 c_{3,m}(c_{2,s,max} - c_{2,s}), \quad (11)$$

which is consistent with the second order hybridization kinetics assumed in Eq. (3a). Note, however, that if $c_{2,s}$ is significantly lower than $c_{2,s,max}$ then the bracketed term in Eq. (11) can be absorbed into the k_3^1, resulting in quasi-first order kinetics.

A similar approach can be used to determine the rate of reaction, R_2, for hybridization of a nonspecifically adsorbed target. In Eq. (12), F_2 represents the flux of adsorbed molecules to a probe, P_a and P_r now represent the equivalent surface-phase probabilities, and P_p has a slightly different meaning in that it represents the ratio of the perimeter of the probe area to the total area per probe,

$$R_2 = F_2 P_p P_a P_r. \quad (12)$$

Analogous to Eq. (5) the number of collisions between a Brownian particle and a line of unit length in two dimensions is given by [32]

$$F_2 = \frac{\langle v \rangle_2 c_{2,ns}}{\pi}. \quad (13)$$

Using Eqs. (6) and (7) above, Eq. (14) is obtained,

$$F_2 = \frac{4D_2 c_{2,ns}}{\pi\sigma_2}. \quad (14)$$

We multiply this by the perimeter of the probe $2\pi R_p$ to determine the collision rate for any given probe and divide by A_t to determine the rate per unit area of coverage, yielding

$$F_2 P_p = \frac{8D_2 c_{2,ns} R_p}{A_t \sigma_2}. \quad (15)$$

Recognizing that $A_t = 1/N_v c_{2,s,max}$, and considering the probability that the probe is available for hybridization, the probability of a successful reaction can be written as

$$R_2 = \left[\frac{8D_2 R_p N_v \chi_2}{\sigma_2}\right] c_{2,ns}(c_{2,s,max} - c_{2,s}) = k_2^1 c_{2,ns}(c_{2,s,max} - c_{2,s}), \quad (16)$$

which is again a second order equation, consistent with that described in Eqs. (3a) and (3b).

In principle k_3^1 and k_2^1 can be determined from Eqs. (11) and (16), respectively. However, this would require a description of both σ_n and χ_n. While in principle σ_n could be estimated from the persistence length of the target molecule, the reaction probability, χ_n, is an unknown value that in previous studies has been somewhat arbitrarily assigned. To avoid this difficulty here and to improve the accuracy of the proposed model, the classical Wetmur and Davidson relationship [25] is used as an estimate of the rate of hybridization for bulk-phase targets in the surface film, k_3^1,

$$k_3^1 = 3.5 \times 10^5 \frac{L^{1/2}}{N}, \quad (17)$$

where N is the complexity of the target sequence and L is the number of nucleotide units. In general the complexity of the sequence is taken as the total number of nonrepeating sequences in a DNA strand [25]. In the absence of any steric interference, in which the bulk molecules are able to move freely within the surface film, the above approximation is likely to be valid. In cases of more dense probe spacing or in the presence of a large amount of nonspecifically adsorbed targets, Eq. (17) is likely to overestimate k_3^1. Note that the incorporation of the Wetmur and Davidson relationship into the formulation is not an inherent assumption in the model and simply provides a technique for estimating χ_3. In principle, any empirically determined equation could be used for this purpose.

The variable k_2^1 can be determined from the ratio of the results from Eqs. (11) and (16) and assuming $\chi_2 = \chi_3$ and $\sigma_2 = \sigma_3$,

$$\frac{k_2^1}{k_3^1} = \frac{16}{3\pi}\left(\frac{D_2}{D_3}\right)\left(\frac{1}{R_p}\right), \quad (18a)$$

$$k_2^1 = 3.5 \times 10^5 \frac{16}{3\pi}\frac{L^{1/2}}{N}\left(\frac{D_2}{D_3}\right)\left(\frac{1}{R_p}\right). \quad (18b)$$

Substituting Eqs. (17) and (18) into Eq. (3a), and defining the parameters k^1 and k^{-1} as

$$k^1 = 3.5 \times 10^5 \frac{L^{1/2}}{N}\left(1 + \frac{16}{3\pi}\left(\frac{D_2}{D_3}\right)\left(\frac{1}{R_p}\right)\frac{c_{2,ns}}{c_{3,m}}\right), \quad (19a)$$

$$k^{-1} = k_3^{-1} + k_2^{-1}, \quad (19b)$$

yields Eq. (20),

$$\frac{\partial c_{2,s}}{\partial t} = k^1 c_{3,m}(c_{2,s,max} - c_{2,s}) - k^{-1} c_{2,s}, \tag{20}$$

which can be viewed as a simplified hybridization reaction accounting for both of the proposed hybridization mechanisms. Note, however, that in this case k^1 is no longer constant and changes with the ratio of $c_{2,ns}$ and $c_{3,m}$ from Eq. (19a).

Thermodynamic stability of hybridization and dissociation kinetics

The binding equation, which governs solid-phase hybridization, is given by,

$$[T] + [P] \leftrightarrow [T:P], \tag{21}$$

where [T] is the bulk concentration of targets in the surface film, [P] is the surface concentration of probes, and [T:P] is the surface concentration of target–probe complexes. This corresponds to $c_{3,m}$, $(c_{2,ns,max} - c_{2,s})$ and $c_{2,s}$, respectively, in the notation that is used herein. An equilibrium-binding constant, K_h, that is proportional to the ratio of these quantities can be defined as

$$\frac{[T:P]}{[T][P]} = \frac{c_{2,s,eq}}{c_{3,m,eq}\left(c_{2,s,max} - c_{2,s,eq}\right)} = K_h, \tag{22}$$

where the subscript eq denotes a quantity at equilibrium. It can be shown that $K_h = k^1/k^{-1}$ from the steady-state version of Eq. (20) (i.e., when $\partial c_{2,s}/\partial t = 0$).

The thermodynamic stability of the target–probe complex is governed by the Gibbs free energy of binding, ΔG, as

$$\frac{k^1}{k^{-1}} = \exp\left(\frac{-\Delta G}{RT}\right) = \exp\left(\frac{-\Delta H}{RT} + \frac{\Delta S}{R}\right). \tag{23}$$

For bulk-phase hybridization, the nearest neighbor model developed by Allawi and Santa Lucia Jr. [33–38] can be used to calculate ΔG for any complementary or single-base-pair mismatched duplex [16]. For heterogeneous hybridization, it is well known that the thermodynamic stability deviates more and more from this classical result as the probe density is increased, resulting in a significant shift in both the shape of the melt curve and the melting temperature [8]. As a result, this approximation can be considered accurate only in the limit of low probe density and even then it is likely to introduce some error as other surface effects are not fully considered (e.g., see Forman et al. [20] for a brief discussion). A few other thermodynamic models that are specific to surface hybridization have been proposed [7,39], but these are also not comprehensive in terms of theoretical development.

While Eq. (23) gives us the ratio of k^1 to k^{-1}, for incorporation into Eq. (3a) we require the explicit temperature via an Arrhenius type formulation,

$$k^1(T) = k_0^1 \exp\left[\frac{-E_a}{R}\left(\frac{1}{T} - \frac{1}{T_0}\right)\right], \tag{24a}$$

$$k^{-1}(T) = k_0^{-1} \exp\left[\frac{-E_d}{R}\left(\frac{1}{T} - \frac{1}{T_0}\right)\right], \tag{24b}$$

where k_0^1 and k_0^{-1} are the values of k^1 and k^{-1} at T_0 which should be 25 °C below the melting temperature, corresponding to the conditions imposed by use of the Wetmur and Davidson relationship. Given that either E_a or E_d can be estimated, the remaining unknowns can be determined from Eq. (25),

$$E_a - E_d = \Delta H, \tag{25}$$

which follows from the thermodynamic model shown in Eq. (23). Estimations for either E_a or E_d will be discussed in later sections are they are in general situation specific.

The variable k^{-1} can be estimated from the preceding equations, but an explicit value of k_2^{-1} is required for incorporation into Eq. (3b). To obtain this parameter it will be assumed that at steady state an independent equilibrium exists between (1) the directly hybridized probes and the targets in the bulk solution and (2) the indirectly hybridized probes and the nonspecifically adsorbed target molecules. As a result, both terms in square brackets in Eq. (3a) are zero at equilibrium. The resulting system of three equations at equilibrium and three unknowns, k_3^{-1}, k_2^{-1}, and $c_{2,s,eq}$, can then be solved to determine the unknown kinetic constants.

Nonspecific adsorption kinetics

The final pieces of information required to fully define the system are the equilibrium values of $c_{2,s}$ and $c_{3,m}$ from Eq. (19a) and the values of k_a and k_d. Under the assumption explained in the preceding section, at equilibrium Eq. (3b) reduces to a Langmuirian adsorption isotherm given by Eq. (26),

$$\frac{k_a}{k_d} = K_a = \frac{c_{2,ns,eq}}{c_{3,m,eq}\left(c_{2,ns,max} - c_{2,ns,eq}\right)}. \tag{26}$$

To our knowledge no comprehensive theory is available for predicting the values of the unknowns in Eq. (26) for oligonucleotides. Chan et al. [40,41] have performed several experimental studies in which they measured the equilibrium relationship between $c_{2,ns,eq}$ and $c_{3,m,eq}$ as well as k_d on various types of glass substrate. From their data the value of K_a can be estimated between 9×10^3 and $12 \times 10^3\,M^{-1}$ and k_d between 0.15 and $0.45\,s^{-1}$, depending on the substrate type. Using these values it is a simple matter to determine k_a from Eq. (26).

To determine the maximum surface concentration of nonspecific adsorption, $c_{2,ns,max}$, a monolayer of adsorbed targets and surface-bound probes can be

assumed (i.e., a full monolayer of targets cannot be adsorbed if some surface area is already taken up by the presence of surface probes). Thus $c_{2,\mathrm{ns,max}}$ is given by

$$c_{2,\mathrm{ns,max}} = \frac{1 - \pi R_{\mathrm{p}}^2 N_{\mathrm{v}} c_{2,\mathrm{s,max}}}{N_{\mathrm{v}} \pi R_{\mathrm{t}}^2}, \tag{27}$$

where R_{t} is the effective radius of an adsorbed target. With the estimate provided by Eq. (27) the relationship between $c_{2,\mathrm{ns,eq}}$ and $c_{3,\mathrm{m,eq}}$ can be determined from Eq. (26), allowing the full definition of the six kinetic constants in Eqs. (3a) and (3b). Thus we have described a complete theory for modeling dynamic heterogeneous hybridization of systems with well-spaced probes.

Experimental validation

There are a few recent experimental studies that have examined dynamic surface-phase hybridization, many of which quote quite different rates of reaction (varying by as much as three orders of magnitude from study to study). Since the bulk-phase transport dynamics outlined in section General theory of coupled transport and surface hybridization/adsorption kinetics are relatively well accepted, the preferred experimental system is one that would effectively eliminate these bulk-phase transport effects from the formulation (i.e., a reaction-limited system) and thus provide a stronger verification of the proposed hybridization model. In addition, the experimental system must have a relatively low probe density to be consistent with the assumptions outlined in the Theory of hybridization kinetics for well-spaced probes section. In the following section we compare the proposed model with experimental results from Zeng et al. [18] for hybridization of dT_{20} probe with fully complementary fluorescein-labeled dA_{20} on an optical fiber functionalized with 3-glycidoxypropyltrimethoxysilane and then investigate some of the interesting predictions of the model.

Hybridization on optical fibers

Details regarding the experimental procedure including fiber preparation and immobilization chemistry are available in Ref. [18], and here we simply mention the experimental details that are required to validate the proposed model. Target delivery was accomplished using a stop-flow liquid-handling system that should have minimized any transport transients. In this study the "low probe density" results are considered, in which the average radius per probe molecule was 18 nm. This distance is sufficiently large to effectively prohibit nearest-neighbor interactions between the immobilized probes, which had an average length (dT_{20} + HEG conjugate) of approximately 10 nm.

As the surface is assumed to be homogeneous and surrounding transport properties are assumed uniform, Eq. (3b) is slightly simplified in that the global surface diffusion term (term 1 in square brackets) can be eliminated from the formulation. A K_{a} value of $9 \times 10^3 1/\mathrm{M}$ and a k_{d} value of 0.3 1/s are selected (at 25 °C) based on the results of Chan et al. [41]. From this same work, the 2D diffusion coefficient for a 21-mer oligonucleotide was found to be on the order of $5 \times 10^{-13}\,\mathrm{m}^2/\mathrm{s}$, and this value is used herein. An interpolation of results presented in Chan et al. [26] was used to estimate the 3D diffusion coefficient at $1.3 \times 10^{-10}\,\mathrm{m}^2/\mathrm{s}$. The remaining kinetic parameters were estimated as outlined in the Theory of hybridization kinetics for well-spaced probes section.

Fig. 2a compares the model predictions with the best-fit experimental results from Zeng et al. [18] for the "low density" case with 0.1 μM targets in 1× PBS solution at 25 °C. As can be seen in Fig. 2a, the model underestimates the initial reaction rate by approximately 25%; however, a good correlation is still observed between the model and the experimental data during the initial stages of hybridization. As equilibrium is approached,

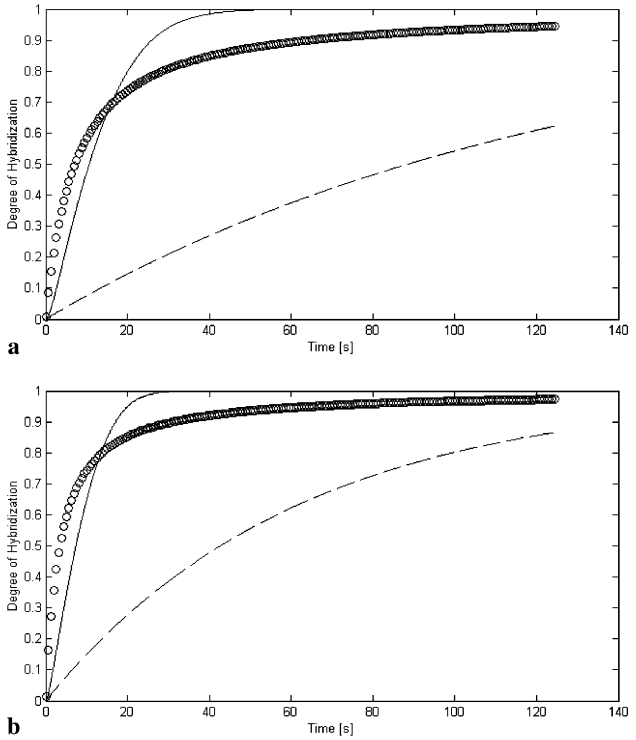

Fig. 2. Comparison between model prediction and experimental results for hybridization of fluorescein-labeled dA_{20} probe with dT_{20} target oligonucleotide at (a) $T = 25\,^{\circ}\mathrm{C}$ and (b) $T = 40\,^{\circ}\mathrm{C}$. The experimental data show the change of fluorescence with time, with time zero being the point of introduction of the target molecules onto the sensor. Solid line represents model prediction, dashed line represents model prediction ignoring surface diffusion enhancement, and circles represent best fit to experimental data. Probe density $\approx 1\,\mathrm{nmol/m^2}$, bulk concentration 0.1 μM.

the model tends to overpredict the rate of hybridization, resulting in full hybridization being reached earlier than was observed experimentally. The overestimation of the reaction rate is likely the result of a number of factors. As was observed in Chan et al. [41], the 2D diffusion coefficient tends to decrease as the surface concentration increases. Thus assuming a static value as was done here is likely to overestimate k_2^1 in these later stages of the reaction. Additionally, the increased surface oligonucleotide concentration is likely to reduce the value of k_3^1 for the reasons outlined in the Theory of hybridization kinetics for well-spaced probes section (i.e., steric interference). As was remarked by Zeng et al. [18], a better fit to these data can be obtained through the use of a higher order reaction model. While the general model of Eqs. (3a) and (3b) could easily be updated to consider higher order reactions, the kinetic variables obtained via the technique outlined in the Theory of hybridization kinetics for well-spaced probes section are in general not globally applicable. Therefore the treatment in this paper is restricted to the lower order case. The dashed line in Fig. 2a represents the predicted hybridization rate ignoring the 2D surface diffusion enhancement (i.e., setting $k_2^1 = 0$ and $k_2^{-1} = 0$). It is apparent that ignoring this surface diffusion effect will result in significant underestimation of the reaction rate.

Fig. 2b compares the best-fit experimental results, again from Zeng et al. [18], with the model predictions for the case similar to that described in Fig. 2a but at $T = 40\,^{\circ}\mathrm{C}$. The results of Koval et al. [9] are used to estimate the value of E_a from Eq. (25), which was approximately 8 kcal/mol. The 2D and 3D diffusion coefficients were also adjusted for temperature effects using the Einstein relation. As in the previous case the model prediction and experimental results match reasonably well during the initial stages of hybridization, with a slight overprediction in the rate of hybridization near completion of equilibration.

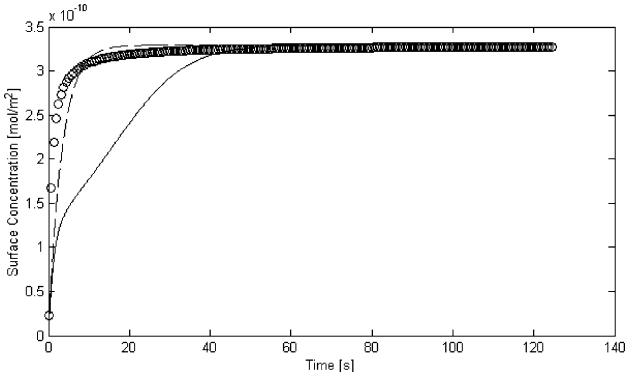

Fig. 3. Predicted adsorption isotherms for fully noncomplementary targets (dashed line) and fully complementary probes (solid line) compared with experimental results for fully noncomplementary adsorption (circles).

Fig. 3 shows the predicted adsorption isotherms for noncomplementary dT_{20} target (dashed line) and complementary dA_{20} targets (solid line) compared with best-fit experimental results [18] for the fully noncomplementary adsorption of fluorescein-labeled dT_{20} (circles). In both simulated cases the maximum surface concentration from Eq. (25) was determined to be 0.36 $\mu\mathrm{mol/m^2}$. For the experimental results, the fluorescence units were converted to a surface concentration by scaling using the predicted equilibrium surface concentration value. The fit between the noncomplementary cases is quite good; with the simulated prediction only marginally lagging behind the experimental result. The complementary hybridization case shows the depletion in the concentration of nonspecifically adsorbed targets (within the transient stage) as a result of their transition to a hybridized state.

Comments on some other published experimental results

In the cases shown above, we have typically observed and predicted kinetic variables (k_3^1, k_2^1) on the order of 10^6 1/M s. By comparison Okahata et al. [10] observed a hybridization constant (in our terminology comparable to k^1) on the order of 10^5 1/M s for a 20-mer oligonucleotide using a bulk solution concentration of 0.19 μM and a probe density on the order of 200 nmol/m^2. Henry et al. [15] observed a similar k^1 at the lowest surface probe density they investigated of 20 nmol/m^2. Peterson et al. [16] observed slower reaction rates taking on the order of 30 min to obtain complete hybridization with a bulk target concentration of 1 μM and probe densities varying from 30 to 200 nmol/m^2. One reason for the enhanced rate of reaction observed and predicted in this study is the significantly lower probe density of $\approx$1 nmol/m^2. As is shown in Fig. 4, the model predicts a significant decrease in the rate of hybridization with

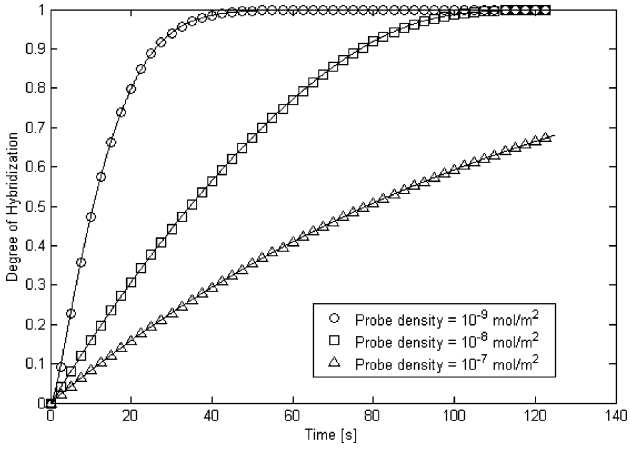

Fig. 4. Predicted influence of surface probe density on rate of hybridization.

increasing probe density. This is a result of the lower $c_{2,ns,max}$ from Eq. (27) for the high probe density case. Furthermore, the depletion effect shown in Fig. 3 becomes enhanced as the total number of probe molecules that are available for hybridization is greater. An additional probe spacing effect that is not reflected in Fig. 4 stems from the fact that the Wetmur and Davidson approximation is likely to overestimate k_3^1 when probe–probe interactions are present.

Finite element simulations of hybridization on temperature gradient surfaces

In this section the theory developed and verified above will be incorporated into the BLOCS finite element-based microfluidics code [31] and used to model the coupled transport, adsorption, and hybridization in a microfluidics-based biosensor with an imposed surface temperature gradient. A schematic of the sensor surface is shown in Fig. 5. For the purposes of these initial simulations it will be assumed that the sensor has a surface area 10 by 10 mm square, a channel height of 200 μm, and a uniform probe spacing and that the solution containing the target molecules is delivered by fully developed pressure-driven flow resulting in the parabolic velocity profile shown in Fig. 5. The inlet target concentration is maintained constant throughout the simulation and a zero flux boundary condition is applied along all nonreacting surfaces.

Numerical method

The BLOCS microfluidics code has been used in a number of recent studies to investigate a variety of three-dimensional microfluidic, microtransport, and microthermal processes such as microscale mixing [31], flow over electrokinetically heterogeneous surfaces [42], and the thermal modeling of a PCR microchip [43]. This study, however, represents the first application of the code in a coupled transport and surface reaction formulation. In essence the BLOCS code discretizes the 3D bulk computational domain using 27-noded 3D brick elements and makes use of triquadratic basis functions. Analogous to the bulk domain, the 2D surface domain is discretized using 9-noded 2D elements and biquadratic basis functions [44]. Both the 3D transient convection diffusion and the 2D transient diffusion–adsorption–reaction problems are discretized in time using an implicit first order Euler scheme and solved using an iterative biconditioned stabilized conjugate gradient method. A typical transient simulation with 7875 bulk-phase nodes and 525 surface nodes required approximately 1 h to compute on a 2000-MHz PC with 1000 Mbyte of RAM. For further details on the numerical code the reader is referred to Ref. [31].

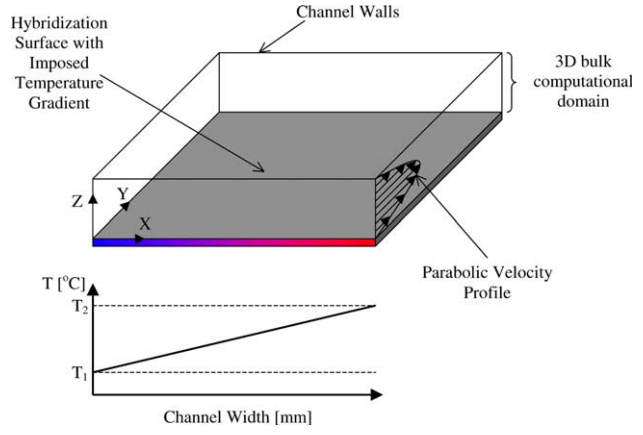

Fig. 5. Geometry of microfluidics-based biosensor showing temperature gradient and parabolic velocity profile.

Hybridization of fully complementary dT_{20}:dA_{20}

For the initial simulation the sensor surface of Fig. 5 is considered to have a 20 °C temperature gradient along the x axis ($T_{min} = 40$ °C and $T_{max} = 60$ °C). The target concentration at the inlet to the sensor channel is 0.1 μM and the maximum fluid velocity is 0.5 mm/s, which corresponds to a Reynolds number in the range of 0.1 for aqueous solutions at these temperatures. The diffusion coefficients and kinetic variables were all corrected for local temperature variations using the techniques outlined in the Theory of hybridization kinetics for well-spaced probes and Experimental validation sections. As in the Experimental validation section, hybridization is considered for dT_{20} probes and dA_{20} targets which have a melting temperature under these conditions of 51 °C [35–38].

Fig. 6 illustrates the coupling between the three-dimensional bulk-phase target transport (transparent white contours) and the surface-phase hybridization (solid surface contours). As expected, the reaction is seen to be proceeding along the sensor length from left to right as the targets are convected along the length of the channel. Since the range of the applied temperature gradient spans the melt temperature of the target–probe duplexes, a significant reduction in the duplex concentration is observed at the hotter end of the channel ($x = 10$ mm). Surface concentration contours are more closely examined in Fig. 7, which shows the changes in the total surface concentration of targets (hybridized and nonspecifically adsorbed) with time. The influence of nonspecific adsorption is clearly visible in Fig. 7, particularly near the hot end of the channel where the hybridized concentration is negligible.

Fig. 8 shows the bulk concentration profile at (8a) the 40 °C end of the channel ($x = 0$ mm) and (8b) the 60 °C end of the channel ($x = 10$ mm). Of interest is the asymmetry that exists in the concentration profiles

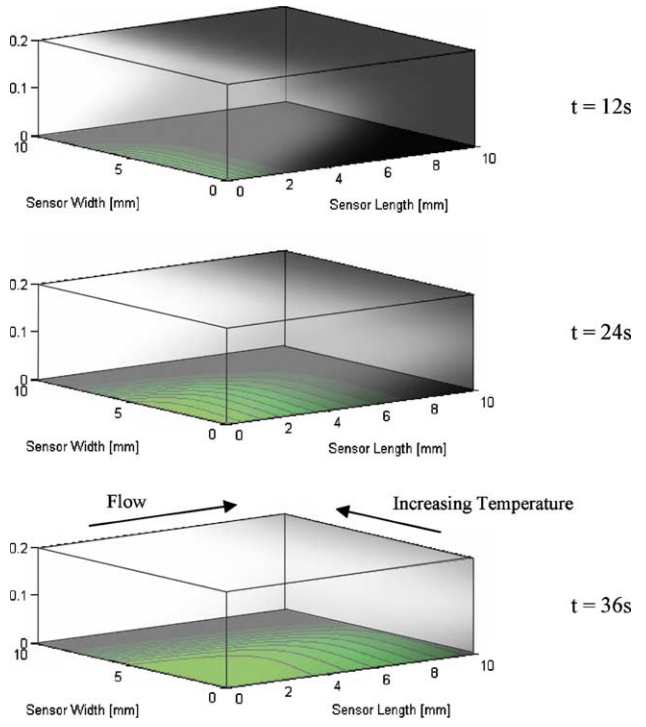

Fig. 6. Simulated dynamic hybridization in microfluidics-based biosensor with a 20 °C surface temperature gradient ($T_{min} = 40$ °C, $T_{max} = 60$ °C). Transparent white contours in the channel represent bulk target concentration and the surface contours show degree of hybridization.

about the center axis in Fig. 8a and b. The reaction takes place only along the bottom surface and the local concentration is reduced as targets become adsorbed on the surface, resulting in the asymmetrical concentration profiles. Through close comparison of the two profiles it can be seen that the local concentrations (especially near the sensor surface) tend to be lower at the 40 °C profile, as there is both hybridization and nonspecific adsorption in this region.

Comparison of fully complementary and single-base-pair mismatch

In Fig. 9 the total surface concentration profiles are compared for fully complementary, dT_{20}:dA_{20}, and single-base-pair mismatch, dT_{20}:$d(A_9TA_{10})$, hybridization. As mentioned above the fully complementary set has a melting temperature of 51 °C vs 44 °C [35–38] for the noncomplementary set. The presence of the temperature gradient exploits the differences in the thermodynamic stability of the duplex, resulting in significantly different transient and steady-state concentration patterns. This demonstrated the potential of the temperature gradient technique as a method of discriminating against base-pair mismatches, and a unique surface concentration pattern is formed for each case.

Influence of target concentration, delivery speed, and channel height on hybridization time

The numerical technique allows the quantitative prediction of how changes in the biochip operating conditions or design will affect the fluorescence signal

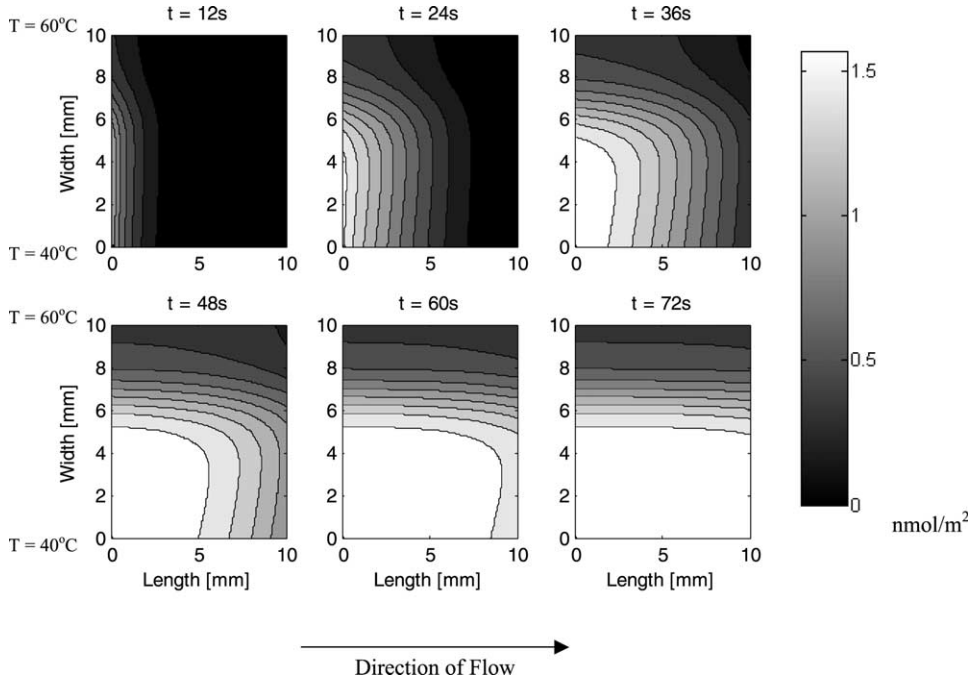

Fig. 7. Predicted total surface concentration profiles (nonspecifically and specifically adsorbed) for biochip surface with 20 °C temperature gradient ($T_{min} = 40$ °C, $T_{max} = 60$ °C).

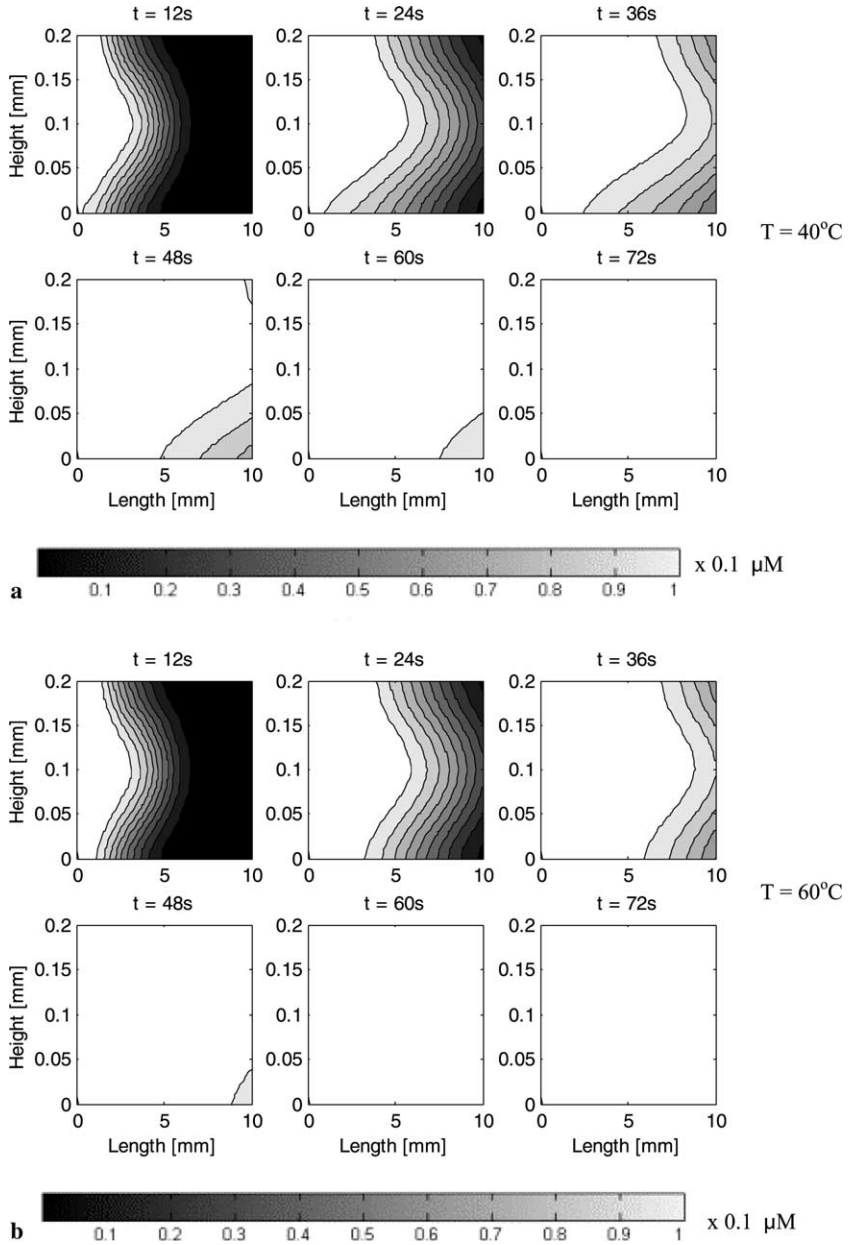

Fig. 8. Predicted bulk concentration profiles along sidewalls of biosensor with 20 °C temperature gradient ($T_{min} = 40$ °C, $T_{max} = 60$ °C). (a) Bulk concentration profiles at $x = 0$ mm ($T = 40$ °C). (b) Bulk concentration profiles at $x = 10$ mm ($T = 60$ °C).

output. Of particular interest from an operational standpoint is how the target concentration, delivery speed, and channel height will affect the length of time that is required to reach an effective steady-state surface concentration pattern (defined as a 99% match with the surface concentration pattern at infinite time). Fig. 10 shows the influence of bulk target concentration on the time required to reach steady state for three different target delivery speeds (again using the dT_{20}:dA_{20} probe–target complex). As expected, increasing the target concentration does tend to reduce the time required to reach a steady state. However, at concentrations above 0.1 μM this difference essentially becomes insignificant. Above this concentration the limiting step is the reaction itself, while below this concentration the reaction is limited by target transport (i.e., 0.1 μM represents the transition point between a transport-limited and a reaction-limited system). Also from Fig. 10 it can be observed that at the slowest delivery speed the reaction rate is effectively governed by the length of time required to convect the targets across the length of the sensor surface. As the delivery speed is increased, the time decreases. A 10-fold increase in the delivery speed from Re = 0.1 to Re = 1.0 results in only a 2-fold decrease in the reaction time at 0.1 μM target concentration.

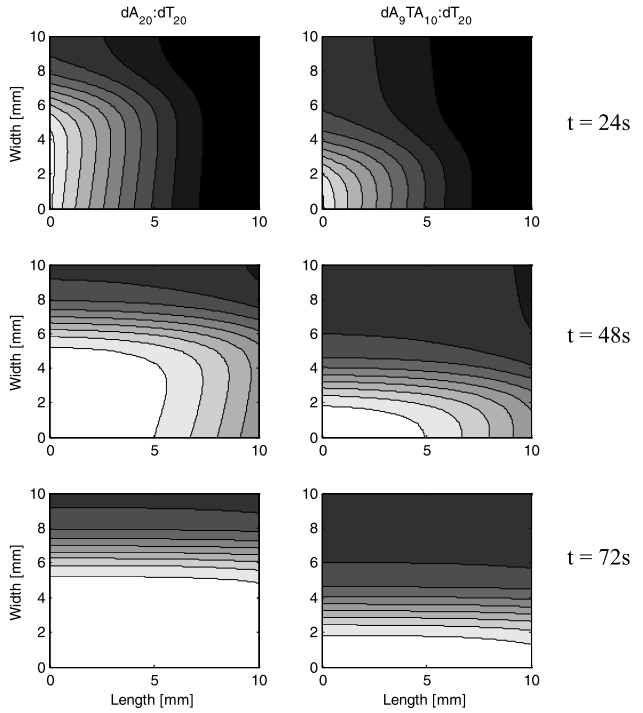

Fig. 9. Comparison between surface concentration profiles between a fully complementary probe–target complex (dT_{20}:dA_{20}) and a probe–target complex containing a single-base-pair mismatch (dT_{20}:dA_9TA_{10}).

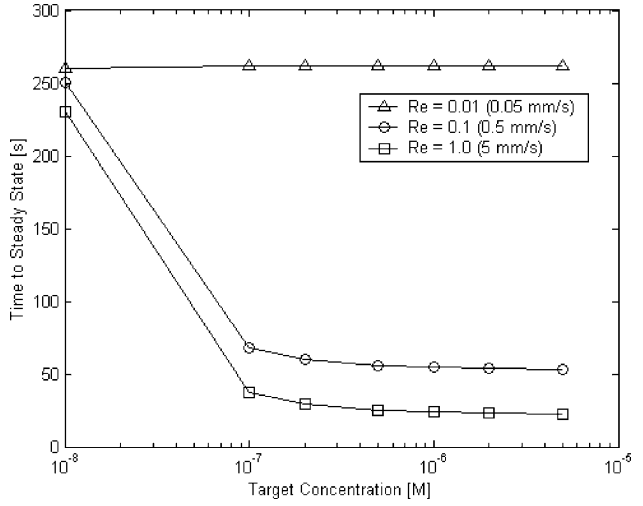

Fig. 10. Influence of bulk target concentration on the time required to reach a steady-state surface concentration pattern in a 200-μm channel at delivery speeds of Re = 0.01 (0.05 mm/s), Re = 0.1 (0.5 mm/s), and Re = 1 (5 mm/s).

In Fig. 11 the influence of channel height on the time required to reach a steady-state fluorescence signal is considered. Rather than fix the Reynolds number, which is dependent on the channel height, the delivery speed has been fixed at 0.5 mm/s, and the calculations presume a bulk target concentration of 0.1 μM. Decreasing the

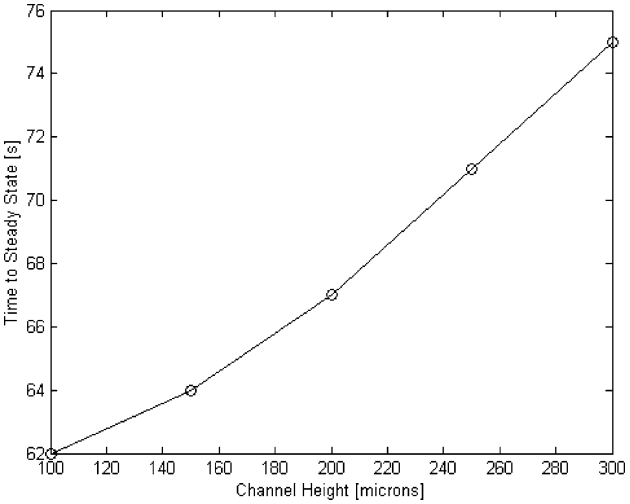

Fig. 11. Influence of channel height on the time required to reach a steady-state surface concentration pattern at a bulk target concentration of 0.1 μM and a 0.5 mm/s delivery speed.

channel height tends to decrease the time required to reach the steady-state concentration profile. This is a result of faster convection near the surface in smaller channels, due to the parabolic velocity profile, which tends to reduce the magnitude of the target depletion zones (shown in Fig. 8) and increases the overall rate of reaction.

Summary and conclusions

The high degree of selectivity available from heterogeneous hybridization of surface-bound probe oligonucleotides with solution-phase targets makes it a particularly attractive mechanism for use in biosensors and biochips. The development of optimized, highly selective biochips that can exploit hybridization for target detection in conjunction with microfluidics for sample handling requires the development of advanced numerical models and a fundamental understanding of the kinetics and thermodynamics of solid-phase duplex formation.

In this study a general theory for modeling solid-phase hybridization has been developed, based on a two-mechanism approach in which surface-bound probes can hybridize with a target directly from the bulk or indirectly through an initial nonspecific adsorption step and subsequent surface diffusion to the probe. For the special case of well-spaced noninteracting probes, a technique for estimating the kinetic parameters involved in the general theory has been developed and experimentally verified. Based on the comparison between the experimental data and theoretical predictions it was observed that the proposed model works quite well; however, it is noted that a higher order model may produce an even better result. It is also shown that an

increase in probe density will lead to slower reaction rates, as has been observed experimentally in a number of cases.

The experimentally verified theory was then implemented as part of the BLOCS finite element microfluidics code developed in our lab and used to model the dynamic hybridization biochip surface with a temperature gradient. It is shown how such a device can exploit the differences between the thermodynamic stability of a fully complementary duplex and that of a noncomplementary duplex to distinguish between the two by producing a unique surface concentration pattern for each. Using these numerical simulations it is shown how the dynamic transport of the targets is likely to affect the rate and location of hybridization. It is also demonstrated that although nonspecific hybridization is present the change in the concentration of hybridized targets over the sensor platform is sufficiently high to allow the distinction between a fully complementary duplex and a noncomplementary duplex. Additionally, these simulations have allowed us to determine the optimum transport speed, target concentration, and channel height. The results presented here will aid in the interpretation of results obtained with such a temperature gradient biochip.

Appendix A. Nomenclature

Variables

A_p	Area of the probe site, m^2.
A_t	Total area per probe site, m^2.
$c_{2,s}$	Surface-phase concentrations of specifically (hybridized) adsorbed target molecules, mol/m^2.
$c_{2,s,max}$	Concentration of surface-bound probes, mol/m^2.
$c_{2,ns}$	Surface-phase concentration of nonspecifically adsorbed target molecules.
$c_{2,ns,max}$	Maximum surface-phase concentration of nonspecifically adsorbed target molecules, mol/m^2.
c_3	Solution-phase concentration of targets, M.
$c_{3,m}$	Solution-phase concentration of targets in the surface film, M.
D_2	Two-dimensional (i.e., surface phase) diffusion coefficient, m^2/s.
D_3	Three-dimensional (i.e., solution phase) diffusion coefficient, m^2/s.
E_a	Activation energy for hybridization, kcal/mol.
E_d	Activation energy for denaturing, kcal/mol.
eq	Subscript denoting quantity at equilibrium.
F_2	Flux of adsorbed target molecules that collide with a probe, mol/ms.
F_3	Flux of bulk-phase target molecules that collide with the surface, $mol/m^2\,s$.
k^1	Kinetic association constant for hybridization (direct and indirection), 1/M s.
k^{-1}	Kinetic disassociation constant for hybridization (direct and indirection), 1/M s.
k_0^1	Kinetic association constant for hybridization (direct and indirection) at $T = T_0$, 1/M s.
k_0^{-1}	Kinetic disassociation constant for hybridization (direct and indirection) at $T = T_0$, 1/M s.
k_3^1	Kinetic association constant for direct hybridization (from solution phase), 1/M s.
k_3^{-1}	Kinetic disassociation constant for direct hybridization (from solution phase), 1/s.
k_2^1	Kinetic association constant for indirect hybridization (from surface phase), 1/M s.
k_2^{-1}	Kinetic disassociation constant for indirect hybridization (from surface phase), 1/s.
k_a	Kinetic association constant for nonspecific adsorption, 1/M s.
k_d	Kinetic disassociation constant for nonspecific adsorption, 1/s.
K_a	Equilibrium constant for Langmuirian-type nonspecific adsorption, 1/M.
K_h	Equilibrium binding constant for hybridization, 1/M.
L	Length of the target sequence.
N	Complexity of the target sequence.
N_v	Avagadro's Number, 1/mol.
P_a	Probability that that probe is available for hybridization.
P_p	Probability that the collision location is a probe site.
P_r	Probability that a collision will result in successful hybridization.
R	"Gas" constant, kcal/mol K.
R_2	Reaction rate for indirect hybridization, $mol/m^2\,s$.
R_3	Reaction rate for direct hybridization, $mol/m^2\,s$.
R_p	Radius of probe site, m.
T	Temperature, K.
n	Vector normal to the surface.
t	Time, s.
v	Velocity, m/s.

Greeks

χ_n	Probability that the nth-dimensional collision will result in successful hybridization.
σ_n	Frequency of collisions in n dimensions, 1/s.
ζ_n	Run between collisions (Brownian persistence distance) in n dimensions, m.
ΔG	Gibbs free energy of binding, kcal/mol.

Appendix A. (*continued*)

ΔH	Binding enthalpy, kcal/mol.
ΔS	Binding entropy, kcal/mol K.

Miscellaneous

$\langle v \rangle_n$	Instantaneous speed of a Brownian target in n dimensions, m/s.
[T]	Bulk-phase concentration of targets in the surface film, mol/m^3.
[P]	Surface concentration of probes, mol/m^3.
[T:P]	Surface concentration of target–probe complexes.

Acknowledgments

The authors are grateful for financial support from the Natural Sciences and Engineering Research Council through a scholarship to D. Erickson and through a research grant to D. Li and U.J. Krull.

References

[1] X. Li, W. Gu, S. Mohan, D.J. Baylink, DNA microarrays: their use and misuse, Microcirculation 9 (2002) 13–22.
[2] M. Gabig, G. Wegrzyn, An introduction to DNA chips: principles technology applications and analysis, Biochem. Pol. 48 (2001) 615–622.
[3] J. Wang, From DNA biosensors to gene chips, Nucleic Acid Res. 28 (2000) 3011–3016.
[4] M. Thompson, L.M. Furtado, High density oligonucleotide and DNA probe arrays for the analysis of target DNA, Analyst 124 (1999) 1133–1136.
[5] B. Lemieux, A. Aharoni, M. Schena, Overview of DNA chip technology, Mol. Breeding 4 (1998) 277–289.
[6] J.H. Watterson, P.A.E. Piunno, C.C. Wust, U.J. Krull, Effects of oligonucleotide immobilization density on selectivity of quantitative transduction of hybridization of immobilized DNA, Langmuir 16 (2001) 601–608.
[7] P.A.E Piunno, J.H. Watterson, C.C. Wust, U.J. Krull, Considerations for the quantitative transduction of hybridization of immobilized DNA, Anal. Chem. Acta 400 (1999) 73–89.
[8] J.H. Watterson, P.A.E. Piunno, U.J. Krull, Towards the optimization of an optical DNA sensor: control of selectivity coefficients and relative surface affinities, Anal. Chem. Acta 457 (2002) 29–38.
[9] V.V. Koval, O.V. Gnedenko, Y.D. Ivanov, O.S. Fedorova, A.I. Archakov, D.G. Knorre, Real-time oligonucleotide hybridization kinetics monitored by resonant mirror technique, IUBMB Life 48 (1999) 317–320.
[10] Y. Okahata, M. Kawase, K. Niikura, F. Ohtake, H. Furusawa, Y. Ebara, Kinetic measurements of dna hybridization on an oligonucleotide-immobilized 27-MHz quartz crystal microbalance, Anal. Chem. 70 (1998) 1288–1296.
[11] M. Jobs, S. Fredriksson, A.J. Brookes, E. Landegren, Effect of oligonucleotide truncation on single-nucleotide distinction by solid-phase hybridization, Anal. Chem. 74 (2002) 199–202.
[12] P.V. Riccelli, F. Merante, K.T. Leung, S. Bortolin, R.L. Zastawny, R. Janeczki, A.S. Benight, Hybridization of single-stranded DNA targets to immobilized complementary DNA probes: comparison of hairpin versus linear capture probes, Nucleic Acids Res. 29 (2001) 996–1004.
[13] J. Yguerabide, A. Ceballos, Quantitative fluorescence method for continuous measurement of DNA hybridization kinetics using a fluorescent intercalator, Anal. Biochem. 228 (1995) 208–220.
[14] P.W. Stevens, M.R. Henry, D.M. Kelso, DNA hybridization on microparticles: determining capture-probe density and equilibrium dissociation constants, Nucleic Acids Res. 27 (1999) 1719–1727.
[15] M.R. Henry, P.W. Stevens, J. Sun, D.M. Kelso, Real-time measurements of DNA hybridization on microparticles with fluorescence resonance energy transfer, Anal. Biochem. 276 (1999) 204–214.
[16] A.W. Peterson, R.J. Heaton, R.M. Georgiadis, The effect of surface probe density on DNA hybridization, Nucleic Acids Res. 29 (2001) 5163–5168.
[17] J.H. Watterson, P.A.E. Piunno, C.C. Wust, S. Raha, U.J. Krull, Influences on nonselective interactions of nucleic acids on response rates of nucleic acid fiber optic biosensors, Fresenius J. Anal. Chem. 369 (2001) 601–608.
[18] J. Zeng, A. Almadidy, J. Watterson, U.J. Krull, Interfacial hybridization kinetics of oligonucleotides immobilized onto fused silica surfaces, Sens. Actuators (2002) in press.
[19] F.F. Bier, F. Kleinjung, F.W. Scheller, Real-time measurement of nucleic-acid hybridization using evanescent-wave sensors: steps towards the genosensor, Sens. Actuators B 38–39 (1997) 78–82.
[20] J.E. Forman, I.D. Walton, D. Stern, R.P. Rava, M.O. Trulson, Thermodynamics of duplex formation and mismatch discrimination on photolithographically synthesized oligonucleotide arrays, in: N.B. Leontis, J. SantaLucia Jr. (Eds.), Molecular Modeling of Nucleic Acid, Am. Chem. Soc., Washington, DC, 1998, pp. 206–228.
[21] J. Meinkoth, G. Wahl, Hybridization of nucleic acids immobilized on solid supports, Anal. Biochem. 138 (1984) 267–284.
[22] M.M. Anderson, Hybridization Strategym, in: B.D. Hames, S.J. Higgins (Eds.), Gene Probes 2: A Practical Approach, Oxford Univ. Press, Oxford, 1995, pp. 1–29.
[23] G.H. Keller, Molecular Hybridization Technology, in: G.H. Keller, M.M. Manak (Eds.), DNA Probes, second ed., Stockton Press, New York, 1993, pp. 1–25.
[24] R.W. Titball, D.J. Squirrell, Probes for nucleic acids and biosensors, in: E. Kress-Rogers (Ed.), Handbook of Biosensors and Electronic Noses: Medicine, Food, and the Environment, CRC Press, Boca Raton, FL, 1997, pp. 91–109.
[25] J.G. Wetmur, N. Davidson, Kinetics of renaturation of DNA, J. Mol. Biol. 31 (1968) 349–370.
[26] V. Chan, D.J. Graves, S.E. McKenzie, The biophysics of DNA hybridization with immobilized oligonucleotide probes, Biophys. J. 69 (1995) 2243–2255.
[27] D. Axelrod, M.D. Wang, Reduction-of-dimensionality kinetics at reaction-limited cell surface receptors, Biophys. J. 66 (1994) 588–600.
[28] A. Sadana, A. Ramakrishnan, A fractal analysis approach for the evaluation of hybridization kinetics in biosensors, J. Colloid Int. Sci. 234 (2001) 9–18.
[29] M.L. Yarmush, D.B. Patankar, D.M. Yarmush, An analysis of transport resistances in the operation of BIAcore^{TM}: implications for kinetic studies of biospecific interactions, Mol. Immunol. 33 (1996) 1203–1214.
[30] M.A. Livshits, A.D. Mirzabekov, Theoretical analysis of the kinetics of dna hybridization with gel-immobilized oligonucleotides, Biophys. J. 71 (1996) 2795–2801.
[31] D. Erickson, D. Li, Influence of surface heterogeneity on electrokinetically driven microfluidic mixing, Langmuir 18 (2002) 1883–1892.
[32] F. Reif, Fundamentals of Statistical and Thermal Physics, McGraw–Hill, New York, 1965.

[33] J. SantaLucia Jr., H.T. Allawi, P.A. Seneviratne, Improved nearest-neighbor parameters for predicting DNA duplex stability, Biochemistry 35 (1996) 3555–3562.
[34] N. Peyret, P.A. Seneviratne, H.T. Allawi, J. SantaLucia Jr., Nearest-neighbor thermodynamics and NMR of DNA sequences with internal A · A, C · C, G · G, and T · T mismatches, Biochemistry 38 (1999) 3468–3477.
[35] H.T. Allawi, J. SantaLucia Jr., Nearest-neighbor thermodynamics of internal A · C mismatches in DNA: sequence dependence and ph effects, Biochemistry 37 (1998) 9435–9444.
[36] H.T. Allawi, J. SantaLucia Jr., Thermodynamics of internal C · T mismatches in DNA, Nucleic Acids Res. 26 (1998) 2694–2701.
[37] H.T. Allawi, J. SantaLucia Jr., Nearest neighbor thermodynamic parameters for internal G · A mismatches in DNA, Biochemistry 37 (1998) 2170–2179.
[38] H.T. Allawi, J. SantaLucia Jr., Thermodynamics and NMR of internal G · T mismatches in DNA, Biochemistry 36 (1997) 10581–10594.
[39] A. Vainrub, B.M. Pettitt, Thermodynamics of association to a molecule immobilized in an electric double layer, Chem. Phys. Lett. 323 (2000) 160–166.
[40] V. Chan, D. Graves, P. Fortina, S.E. McKenzie, Adsorption and surface diffusion of DNA oligonucleotides at liquid/solid interfaces, Langmuir 13 (1997) 320–329.
[41] V. Chan, S.E. McKenzie, S. Surrey, P. Fortina, D.J. Graves, Effects of hydrophobicity and electrostatics on adsorption and surface diffusion of DNA oligonucleotides at liquid/solid interfaces, J. Colloid. Int. Sci. 203 (1998) 197–207.
[42] D. Erickson, D. Li, Microchannel flow with patchwise and periodic surface heterogeneity, Langmuir 18 (2002) 8949–8959.
[43] D. Erickson, D. Li, 3D numerical simulations of a microchannel thermal cycling reactor, Int. J. Heat Mass Trans. 45 (2002) 3759–3770.
[44] J.C. Heinrich, D.W. Pepper, Intermediate Finite Element Method, Taylor & Francis, Philadelphia, 1999.